The variable radio counterpart of *Swift* J1858.6-0814

J. van den Eijnden[1]*, N. Degenaar,[1] T. D. Russell[1] ,[1] D. J. K. Buisson,[2] D. Altamirano,[2] M. Armas Padilla[3,4], A. Bahramian[5,6], N. Castro Segura[2], F. A. Fogantini,[7,8] C. O. Heinke[9], T. Maccarone,[10] D. Maitra,[11] J. C. A. Miller-Jones[6], T. Muñoz-Darias[3,4], M. Özbey Arabacı,[2,12] D. M. Russell[13], A. W. Shaw[9,14], G. Sivakoff,[9] A. J. Tetarenko[15], F. Vincentelli[2] and R. Wijnands[1]

Affiliations are listed at the end of the paper

ABSTRACT

Swift J1858.6-0814 is a transient neutron star X-ray binary discovered in 2018 October. Multiwavelength follow-up observations across the electromagnetic spectrum revealed many interesting properties, such as erratic flaring on minute time-scales and evidence for wind outflows at both X-ray and optical wavelengths, strong and variable local absorption, and an anomalously hard X-ray spectrum. Here, we report on a detailed radio observing campaign consisting of one observation at 5.5/9 GHz with the Australia Telescope Compact Array, and nine observations at 4.5/7.5 GHz with the Karl G. Jansky Very Large Array. A radio counterpart with a flat to inverted radio spectrum is detected in all observations, consistent with a compact jet being launched from the system. *Swift* J1858.6-0814 is highly variable at radio wavelengths in most observations, showing significant variability when imaged on 3-to-5-min time-scales and changing up to factors of 8 within 20 min. The periods of brightest radio emission are not associated with steep radio spectra, implying they do not originate from the launching of discrete ejecta. We find that the radio variability is similarly unlikely to have a geometric origin, be due to scintillation, or be causally related to the observed X-ray flaring. Instead, we find that it is consistent with being driven by variations in the accretion flow propagating down the compact jet. We compare the radio properties of *Swift* J1858.6-0814 with those of Eddington-limited X-ray binaries with similar X-ray and optical characteristics, but fail to find a match in radio variability, spectrum, and luminosity.

Key words: accretion, accretion discs – stars: individual (Swift J1858.6-0814) – X-rays: binaries.

1 INTRODUCTION

X-ray binaries, wherein a compact object accretes from an orbiting companion star, form excellent laboratories to study both the accretion and ejection of matter. Such systems are often classified based on the mass of the donor star, with low-mass X-ray binaries (LMXBs) typically having a donor star with a mass $<1\,\mathrm{M_\odot}$. While the compact object in some LMXBs persistently accretes from its companion, the majority of systems are instead transients (see for recent catalogues, e.g. Corral-Santana et al. 2016; Tetarenko et al. 2016). These transient LMXBs mostly reside in a quiescent state, interspersed with accretion outbursts typically lasting weeks to months. During these outbursts, LMXBs can reach mass accretion rates around or exceeding the Eddington limit, increasing multiple orders of magnitude in X-ray luminosity over the course of days to weeks (e.g. Done, Gierlinski & Kubota 2007).

X-ray binaries can also launch outflows from the accreted material, which can either take the form of collimated, relativistic jets, or slower, more massive, disc winds. In a typical black hole or neutron star LMXB outburst, the compact jet and disc winds are not observed simultaneously in radio and X-rays (e.g. Fender, Belloni & Gallo 2004; Ponti et al. 2012). Instead, the compact radio jet is launched in the 'hard' state, dominated by non-thermal,

Comptonized X-ray emission (Corbel et al. 2000; Dhawan, Mirabel & Rodríguez 2000; Stirling et al. 2001), while the winds are detected in X-rays (if inclination allows; Ponti et al. 2013; Higginbottom et al. 2017) in the 'soft', disc-dominated state instead. In the soft state, the compact jet is quenched in black hole systems (Fender et al. 2004). In neutron star systems, soft state jets are observed in some sources, while they are quenched in others (Miller-Jones et al. 2010; Gusinskaia et al. 2017; Díaz Trigo et al. 2018). The jet–wind dichotomy becomes less defined, however, when optical wavelengths are included: disc winds have been observed in the optical bands during the hard states of LMXBs, for instance in the black hole transients *Swift* J1357.2-0933 (Charles et al. 2019; Jiménez-Ibarra et al. 2019) and MAXI J1820+070 (Muñoz-Darias et al. 2019).

The relation between the wind and jet outflows is also more complex at the highest, super-Eddington accretion rates. At such rates, both outflow types are often seen simultaneously (e.g. Neilsen & Lee 2009; Homan et al. 2016; Muñoz-Darias et al. 2016; Motta et al. 2017; Allen et al. 2018; van den Eijnden et al. 2019). Super-Eddington accreting black holes often show flaring by several orders of magnitude on seconds to minutes time-scales, in both X-rays and radio bands, where the radio variability is typically associated with the launch of discrete, expanding ejecta (e.g. Rupen, Dhawan & Mioduszewski 2003a, 2004a; Fender, Homan & Belloni 2009; Tetarenko et al. 2017; Miller-Jones et al. 2019). This origin can be inferred either indirectly from steep radio spectra, and a smoothing

out of the variability with increasing delays towards lower observing frequencies, probing further down the outflow (Tetarenko et al. 2019a). Alternatively, it can be inferred more directly by resolving the ejecta with Very-long Baseline Interferometry (e.g. Miller-Jones et al. 2019). Similar behaviour is also seen in neutron star LMXBs when they accrete close to their Eddington limit (Fomalont, Geldzahler & Bradshaw 2001a,b; Homan et al. 2016; Motta & Fender 2019).

In 2018 October, Krimm et al. (2018) reported the discovery of a new Galactic X-ray transient with the *Burst Alert Telescope* (BAT) aboard the *Neil Gehrels Swift Observatory*, hereafter referred to as *Swift* (Gehrels et al. 2004). This new source, named *Swift* J1858.6-0814 (hereafter Sw J1858), was quickly followed up at many wavelengths and also detected at UV (Bozzo et al. 2018; Kennea & Krimm 2018), optical (Vasilopoulos, Bailyn & Milburn 2018), and radio (Bright et al. 2018) wavelengths. At X-ray energies, Sw J1858 showed an extremely hard spectrum up to 10 keV ($\Gamma < 1$) and a faint outburst, with fluxes up to $\sim 10^{-10}$ erg s^{-1} cm^{-2} (Reynolds et al. 2018). On top of this relatively faint emission, Sw J1858 showed strong, brief X-ray flares (Ludlam et al. 2018; Hare et al. 2019) where the observed flux could increase by more than an order of magnitude (up to, for instance, $\sim 3.5 \times 10^{-9}$ erg s^{-1} cm^{-2} in Hare et al. 2020). Such flares which were also identified at optical wavelengths (Baglio et al. 2018; Paice et al. 2018; Rajwade et al. 2018, 2019; Vasilopoulos et al. 2018). In addition, the X-ray spectrum showed evidence of strong local absorption (Reynolds et al. 2018; Hare et al. 2020), and outflows were observed in the optical spectrum (Muñoz-Darias et al. 2020) and inferred from the X-ray spectrum as well (Buisson et al., in preparation).

Sw J1858 has been active for more than a year at the time of writing: it went into Sun constraint three weeks after the first report of the outburst, but appeared out of Sun constraint in a similar state three months later (Rajwade et al. 2019). It has also remained active after a second Sun constraint period in 2019–2020, out of which it emerged in a softer, previously unobserved X-ray state in 2020 February (Buisson et al. 2020a). As noted by several authors (i.e. Paice et al. 2018; Reynolds et al. 2018; Ludlam et al. 2019; Hare et al. 2020; Buisson et al., in preparation), the rich phenomenology observed in the initial state of Sw J1858 overlaps with the properties of the transient black hole LMXBs V404 Cyg (Rodriguez et al. 2015) and V4641 Sgr (Wijnands & van der Klis 2000): the strong optical and X-ray flaring, X-ray spectral shape (e.g. Motta et al. 2017), and evidence for optical winds is observed in all three sources (Muñoz-Darias et al. 2016, 2020; Muñoz-Darias, Torres & Garcia 2018).

While Sw J1858 was in its new X-ray state since 2020 February, *NICER* observed several flares (one of which was also covered by *NuSTAR*) that, upon closer inspection, turn out to be Type-I X-ray bursts (Buisson et al. 2020b). Such bursts are caused by runaway thermonuclear burning of accreted material on the surface of neutron stars (see for reviews, e.g. Lewin, van Paradijs & Taam 1995; Strohmayer & Bildsten 2006; Galloway & Keek 2017). The bursts observed from Sw J1858 are identified as Type-I bursts from their profile, spectrum, and spectral evolution, and therefore unambiguously show that the accretor is a neutron star. One of the bursts reported by Buisson et al. (2020b) shows evidence for photospheric radius expansion, which implies a distance of ~ 15 kpc to Sw J1858 (assuming the burst reaches the Eddington luminosity; see also Buisson et al. in preparation). We will adopt this distance for our work.

Outside of its flares and before the second Sun constraint period, the outburst of Sw J1858 reached X-ray luminosities of $\lesssim 1.5$ per cent $(D/15 \, \text{kpc})^2 \, L_{\text{Edd}}$ for a neutron star accretor. Given this low X-ray luminosity, we triggered a *Swift* X-ray and Karl G. Jansky Very Large Array (VLA) radio monitoring program to study the outbursts of X-ray transients at low X-ray luminosity. This campaign was supplemented by an observation with the Australia Telescope Compare Array (ATCA). Here, we report the results of this study, focusing on the radio variability properties down to minute time-scales. This paper presents the radio campaign in combination with *Swift* monitoring, which acts to place the radio behaviour into the context of the full outburst.

2 OBSERVATIONS AND DATA ANALYSIS

2.1 Radio

The radio observing campaign of Sw J1858 consisted of one initial observation with ATCA, followed by nine observations performed with the VLA. The ATCA observation was taken on 2018 November 8 between 04:58:09.9 and 11:08:59.9 UTC (project code C2601). The telescope was in its extended 6 km (6B) configuration, with antenna 3 offline. We used PKS 1934-638 as the primary calibrator, while the nearby secondary calibrator for all observations was J1832-1035 ($\sim 7°$ separation). Measurements were recorded simultaneously at 5.5 and 9 GHz in standard continuum mode, with 2048 MHz bandwidth each. In this paper, we will refer to this observation as epoch 1. Details on all individual radio observations, including those discussed below, can be found in Table 1.

The nine VLA observations were part of two observing programs, SE0057 and 19A-495. The first six observations were performed in 2018 November, before the first X-ray Sun constraint. The final three observations were obtained in 2019 February, March, and August, respectively. The first eight observations lasted 1 h, including setup and calibration scans, and were taken in *C*-band using 8-bit mode, with two sub-bands centred at 4.5 and 7.5 GHz with 1024 MHz bandwidth each. The final observation had the same setup but lasted for 3.5 h, maximizing the overlap with other observatories during a coordinated observing campaign. Depending on the start time of the observation, we used either J0137+3309 (3C 48) or J1331+3030 (3C 286) as the primary calibrator. We used the same secondary calibrator as for the ATCA observation. The observations were taken in different configurations, covering D, D→C, C, C→B, B, and A. Throughout this paper, we will refer to these nine observations as epochs 2 through 10.

To calibrate and image the time-averaged radio observations, we followed standard procedures using the COMMON ASTRONOMY SOFT-WARE APPLICATION (CASA; McMullin et al. 2007) version 4.7.2. We used a combination of automatic flagging routines and careful manual inspection of the visibilities to remove RFI, and subsequently imaged Stokes I using the multiscale multifrequency CASA-task CLEAN. In order to maximize sensitivity while reducing the sidelobe-effects of a close-by background source, we use a Briggs weighting scheme with the robust parameter set to 0. The source was significantly detected in each epoch in both bands, and we measured flux densities by fitting the point source with an elliptical Gaussian model with the size and shape of the restoring beam in the image plane using IMFIT. The 1σ uncertainty on the flux density was determined as the rms over a close-by, source-free region.

Given the strong X-ray and optical variability of Sw J1858, we also analysed the radio observations on shorter time-scales to explore intra-observational variability. Due to their different instantaneous uv-plane coverage, we applied different approaches to the ATCA and VLA observation. Making use of its good instantaneous uv-plane coverage, we applied an image-plane approach to the VLA observations: using a custom PYTHON-script and manual checks of

Table 1. Overview of the ten radio observations of Sw J1858, with their corresponding quasi-simultaneous *Swift*/XRT X-ray observations. For epoch 1 through 8 and 10, the time difference is less than 1 d. For epoch 9, the two surrounding X-ray epochs are both separated by a ~1.3 d difference. Therefore, we consider both for our X-ray flux measurements. For epoch 10, the three listed *Swift* observations were back-to-back. All listed MJDs represent the start of the observations. ∗In these two epochs, flaring in 3C 48 might have lead to an underestimate of the target flux density by ~7–10 per cent, see Section 2.1 for details.

Epoch	Observatory	Radio MJD	Primary calibrator	Config.	*Swift* ObsID	XRT mode	*Swift* MJD	XRT Exposure (s)
1	ATCA	58430.207	PKS 1934-638	6B	00010955003	WT	58432.619	30
2	VLA	58431.954	J0137+3309 (3C 48)	D	–	–	–	–
3	VLA	58436.072	J0137+3309 (3C 48)∗	D→C	00010955004	WT	58436.478	1870
4	VLA	58437.060	J0137+3309 (3C 48)∗	D→C	00010970002	PC	58437.465	2035
5	VLA	58438.835	J1331+3030 (3C 286)	D→C	00010970003	PC	58439.390	1630
6	VLA	58443.748	J1331+3030 (3C 286)	C	00010955008	PC	58444.304	1960
7	VLA	58443.922	J0137+3309 (3C 48)	C	00010955008	PC	58444.304	1960
8	VLA	58534.498	J1331+3030 (3C 286)	C→B	00010970008	PC	58537.342	995
9	VLA	58566.479	J1331+3030 (3C 286)	B	00010970023/24	PC	58565.104/58567.754	995/945
10	VLA	58701.035	J1331+3030 (3C 286)	A	00010970043/44/45	PC	58701.032	2200

the output, we imaged the two observing bands (4.5 and 7.5 GHz) on a 3-min time-scale to measure the source's light curve. For ATCA, the east–west orientation makes image-plane analysis on time-scales of minutes, at the flux density levels of Sw J1858, unfeasible. Therefore, we instead used uv-plane fitting with the UVMULTIFIT task (Martí-Vidal et al. 2014), using a 5-min time resolution. For both the VLA and ATCA, we attempted several time resolutions and inspected the results to find the time-scale that best balances sensitivity with the ability to observe short-time-scale variations. We settled on a slightly lower ATCA time resolution, given the higher sensitivity of the VLA. The errors on the light curves were calculated in the same way as the averaged flux density in the image-plane analysis, and as the statistical fitting error in the uv-plane analysis. To assess to what degree any observed variability is intrinsic to the target, instead of atmospheric or instrumental effects, we also analysed a nearby background source on the same time-scale for both the VLA and ATCA.

Finally, for both the full and the time-resolved observations, we calculated the radio spectral index α (where $S_\nu \propto \nu^\alpha$). We estimated the error on α using a Monte Carlo simulation, where we randomly draw flux densities at both observing frequencies and recalculate α in total 10^4 times. The 1σ uncertainty on the spectral index was then calculated as the standard deviation of the resulting distribution of spectral indices.

The VLA primary calibrator 3C 48, used in four epochs (see Table 1), has been undergoing flaring behaviour since 2018 January,[1] which can affect the flux scale at the ~5 per cent level. To check whether this affects our observations, we inspected the output CASA logs of the FLUXSCALE task and compared the calibrated flux density of the secondary calibrator between the nine epochs. While the ATCA calibrator data base[2] shows that J1832-1035 remains at a relatively stable 5.5 GHz flux density over time, we measure a slightly decreased flux density during epochs 3 and 4: ~1.36 Jy, compared to ~1.45–1.50 Jy in the remaining epochs, regardless of primary calibrator. Therefore, the measured average flux densities in those two epochs might be underestimated by ~7–10 per cent. However, this will not affect the time-resolved analysis within observations that we present in this paper.

2.2 X-ray

Swift performed an extensive X-ray monitoring campaign of Sw J1858 under ObsIDs 10955, 10970, and 88868. Observations were taken both in the Photon Counting (PC) and Windowed Timing (WT) modes. Before 2018 November 22, when the target went into Sun constraint, 13 X-ray Telescope (XRT) observations with exposures up to 2 ks were performed. The monitoring then resumed on 2019 February 19, as the source was actively accreting as it appeared from Sun constraint, continuing until early 2019 August. As we focus on the radio properties and variability of Sw J1858, we do not perform a detailed X-ray analysis of all *Swift* observations, but instead focus on measuring the X-ray flux around the radio observations. For more detailed analysis of the X-ray spectrum of Sw J1858, we refer the reader to Hare et al. (2020) and Buisson et al. (in preparation).

Due to the faintness of the source, we do not use data from either *Swift*-BAT or *Monitor of All-sky X-ray Image (MAXI)* observations in this work. Instead, we use the available *Swift*/XRT monitoring data to extract a long-term X-ray light curve of the source, in order to place our radio observations in the context of the full outburst. In addition, we extract and fit spectra of the observations taken closest to our radio epochs, in order to measure the quasi-simultaneous X-ray flux. For every *Swift* observation taken closest to a radio observation, we also consider a 100 s resolution light curve to estimate the amount of X-ray variability at that time. All analysed X-ray data are listed in Table 1.

The only *Swift*/XRT observation within 4 d of the ATCA and first VLA observation (i.e. epochs 1 and 2) was merely 30 s long. Therefore, for that observation we converted the X-ray count rate to a flux assuming a X-ray spectral shape typical of Sw J1858 in the remainder of the outburst (see Section 3.3). For epochs 3 to 7, all performed before the Sun constraint when *Swift* observed nearly every day, the analysed X-ray spectra where taken within 24 h of the radio observation. For epochs 8 and 9, performed after the first Sun constraint, *Swift* monitoring was more sparse. Therefore, the radio and X-ray observations at these later times are typically separated by ~1.5–2 d. Finally, three consecutive *Swift* observations were taken simultaneously with the tenth and final epoch.

Swift/XRT spectra, with corresponding background spectra and response files, and light curves (both long-term and of single observations) were obtained using the online data products generator[3]

---

[1]https://science.nrao.edu/facilities/vla/docs/manuals/oss/performance/fdscale

[2]https://www.narrabri.atnf.csiro.au/calibrators/

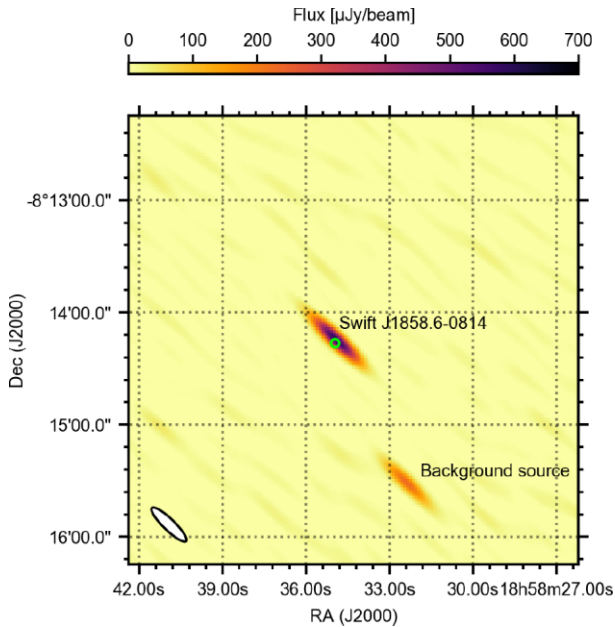[3]http://www.swift.ac.uk/user_objects/

Figure 1. Detection image of epoch 2 at 7.5 GHz. Note the nearby flat-spectrum background source, used to assess the systematic short-time-scale variability of the entire field. The green circle shows the 90 per cent confidence region on the *Swift* X-ray position.

(Evans et al. 2007, 2009). We fit the X-ray spectra with XSPEC v.12.10.1, setting the abundances to Wilms, Allen & McCray (2000) and cross-sections to Verner et al. (1996). We account for interstellar absorption using the TBABS model. Given the low count rates and short observations, we used W-statistics as our fit statistic (Cash 1979). Fluxes with errors were calculated using the convolution model CFLUX. All reported errors are quoted at the 1σ level, unless stated otherwise.

3 RESULTS

3.1 Radio detection and position

Sw J1858 is significantly detected at both radio observing frequencies in every observation. In Fig. 1, we show the radio detection of Sw J1858 during the second epoch at 7.5 GHz (observed with the VLA), when the source was radio brightest. The image shows a radio counterpart consistent with the *Swift*/XRT source. A second, nearby radio source is also visible at a separation of $\sim$2 arcmin, which might contribute to the structured noise reported by AMI-LA (Bright et al. 2018). The best-fitting radio position was measured from the tenth, and final, epoch (7.5 GHz):

RA = 18h58m34.9100s $\pm$ 0.0027s
Dec = $-08°14'14.958'' \pm 0.037''$,

where the error is inferred from the typical astrometric accuracy of the VLA (10 per cent of the synthesized beam). This position is fully consistent with the *Swift*/XRT position reported by Kennea & Krimm (2018). We used the final epoch for this calculation, since the extended A-configuration during this observation yields the smallest statistical uncertainty. While the target was relatively faint during this observation, the high signal-to-noise ($S/N \gg 10$) still ensured the positional accuracy was limited by 10 per cent of the beam size.

3.2 Long-term light curves

In Fig. 2, we show the long-term X-ray and radio light curves, and the radio spectral index as a function of time. Between 30 and 110 d after the outburst detection by BAT, Sw J1858 was in Sun constraint for *Swift*. The X-ray count rate light curve (top) reveals strong variations between observations, changing more than two orders of magnitude. However, no clear outburst profile, with a distinct rise and decay, can be seen. The apparent variability between observations is affected by the presence of X-ray flaring in Sw J1858, which, in combination with the short *Swift* exposures, boosts the count rate in observations covering one or more flares. After day $\sim$135, the dynamic range between observations decreases, with all count rates lying within 1 dex. At the time of writing, Sw J1858 still remains active, much longer than for instance the 2015 outburst of V404 Cyg that it was compared to early on in its outburst (Ludlam et al. 2018; Paice et al. 2018; Reynolds et al. 2018).

The radio light curve, shown in the middle panel, does show an initial peak that decays over time. However, again, the source does not monotonically decay in radio flux density. The radio sampling becomes sparse after the Sun constraint period, but Sw J1858 never decays below $\sim$170 µJy in our observations. All plotted radio flux densities, at both observing frequencies, are listed in Table 2 as well. Finally, we show the radio spectral index as a function of time. In all observations, the spectral index is either consistent with zero or positive, implying a flat or inverted spectrum, respectively. Such a radio spectral shape in an X-ray binary system is consistent with the presence of a compact, steady jet (e.g. Blandford & Königl 1979; Corbel et al. 2004; Fender et al. 2004; Kalemci et al. 2005; Russell et al. 2014). There appears to be no systematic evolution of the spectral index as the radio brightness decays.

3.3 X-ray flux measurements

Alongside the radio flux densities and spectral shape, we also list the measured X-ray fluxes and spectral fit parameters in Table 2. To measure the *observed* fluxes, we fitted every spectrum with a simple phenomenological power-law model, TBABS*PO. First fitting all spectra jointly to measure the absorption column N_H, we find that – *when using this model* – the data does not require the inclusion of interstellar absorption. Hence, we fix N_H to zero in the fits to individual spectra. We stress that this value does not imply a zero column density towards the target; instead, it arises from our non-physical model. Indeed, the measured power-law indices are very hard ($-0.1 < \Gamma < 1.0$), also as a result of our model.

Considering more complex spectral models, Reynolds et al. (2018) showed how *Swift* observation 00010955004 (used in epoch 3) can be better fitted with a complex local absorption model, similar to that seen in V404 Cyg and V4641 Sgr (Morningstar et al. 2014; Motta et al. 2017). Our simple power-law approach, however, can also be applied to the lower-flux spectra; for those spectra, we find that the local absorption model returns large degeneracies between parameters as the spectra are overfitted. Moreover, as we discuss in Section 4.1, there is no systematic difference between the flux measurements obtained from the two models in the observations where both can be applied. Since we aim to determine the observed flux, and discuss the effects of local absorption mostly qualitatively in Section 4.4, we therefore decided on using the power-law model in the analysis of all X-ray spectra.

Two sets of observations, namely radio epochs 1 and 2 (which are the closest to first *Swift* observation), and epoch 9, stand out. First, for epochs 1 and 2, the closest *Swift*/XRT spectrum is merely
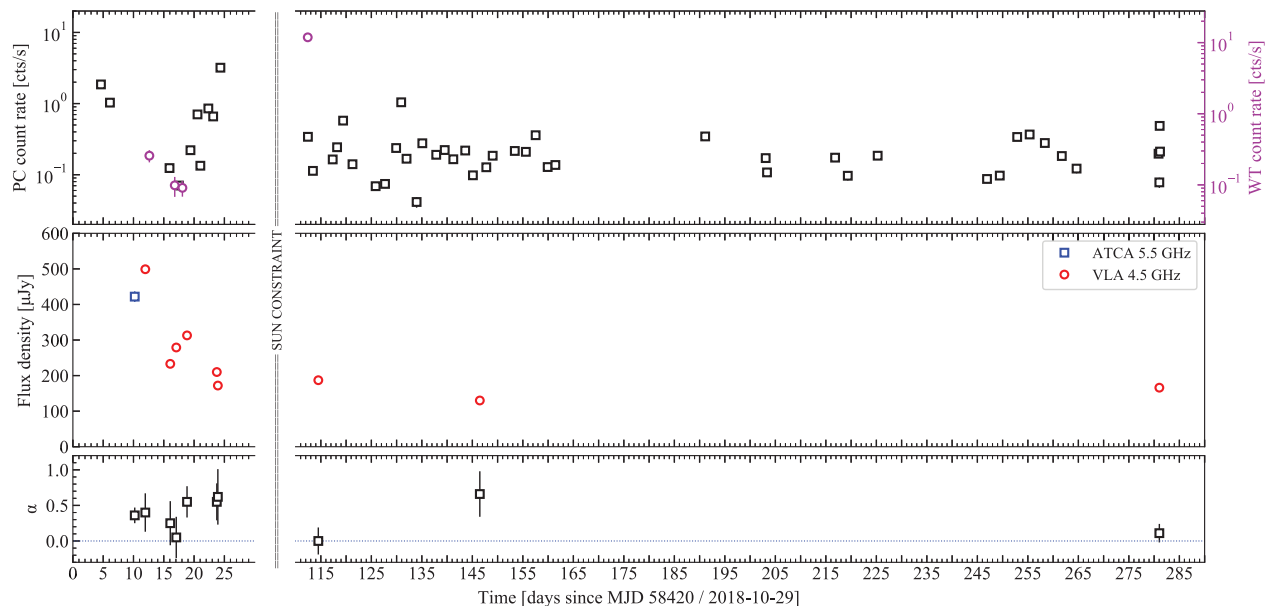
Figure 2. The long-term X-ray, radio, and radio spectral index light curves of the 2018/2019 outburst of Sw J1858. Roughly 30 d after the source's discovery, Sw J1858 went into X-ray Sun constraint for ∼80 d. The top panel shows the *Swift*/XRT count rate in PC mode (black squares) and WT mode (purple circles). The PC and WT axes are offset by 39 per cent, which represent the difference in count rate for the same flux (measured from observations 00010955004 and 00010970002; see Tables 1 and 2). Note that in PC mode, the markers are larger than the uncertainties. The middle panel shows the radio flux density measured with the VLA (4.5 GHz; red circles) and ATCA (5.5 GHz; blue squares). Finally, the bottom panel shows the calculated radio spectral index α. While clear variations in X-ray count rate are visible, no clear rise-decay outburst shape can be distinguished. The radio light curve does show a gradual decrease over time.

Table 2. Radio and X-ray flux (densities) and spectral information. For each radio epoch, we list the low band (4.5 or 5.5 GHz for VLA or ATCA, respectively) and high band (7.5 or 9 GHz) flux density S_ν and the radio spectral index α, where $S_\nu \propto \nu^\alpha$. In the X-rays, we list the measured 0.5–10 keV flux, spectral index Γ, and W-statistic with degrees of freedom. Each *Swift*/XRT spectrum was fitted with a TBABS*POWERLAW model, but N_H was fixed to zero as no absorption was required for any of the fits. ∗In these two epochs, flaring in 3C 48 might lead to an underestimate of the target flux density by ∼7–10 per cent, see Section 2.1 for details.

Epoch	Radio flux density (μJy)		Radio spectral index	0.5–10 keV X-ray flux (erg s^{-1} cm^{-2})	Γ	W_{stat} (dof)
	Low band	High band				
1	422 ± 15	505 ± 15	0.36 ± 0.11	$(2.9 \pm 0.4_{\text{syst}} \pm 1.0_{\text{pois}}) \times 10^{-11}$	N/A (see Section 3.3)	
2	499 ± 12	607 ± 9	0.40 ± 0.18	–	–	–
3∗	233 ± 10	265 ± 10	0.25 ± 0.16	$(1.0 \pm 0.1) \times 10^{-11}$	1.0 ± 0.2	250.6 (265)
4∗	279 ± 10	285 ± 12	0.05 ± 0.14	$(9.5 \pm 1.5) \times 10^{-12}$	−0.1 ± 0.2	127.5 (106)
5	313 ± 9	411 ± 8	0.55 ± 0.24	$(2.3 \pm 0.2) \times 10^{-11}$	0.2 ± 0.1	181.8 (221)
6	210 ± 12	275 ± 11	0.55 ± 0.28	$(1.7 \pm 0.1) \times 10^{-10}$	0.45 ± 0.05	451.3 (507)
7	172 ± 9	233 ± 9	0.62 ± 0.30	$(1.7 \pm 0.1) \times 10^{-10}$	0.45 ± 0.05	451.3 (507)
8	187 ± 12	184 ± 9	0.00 ± 0.19	$(2.1 \pm 0.3) \times 10^{-11}$	0.0 ± 0.2	112.7 (108)
9	130 ± 10	182 ± 8	0.66 ± 0.32	$(1.2 \pm 0.2) \times 10^{-11}$	0.5 ± 0.2	98.1 (91)
10	166 ± 9	176 ± 6	0.11 ± 0.13	$(3.1 \pm 0.2) \times 10^{-11}$	0.2 ± 0.1	256.4 (285)

30 s long. Therefore, instead of fitting the spectrum, we converted the measured WT-mode count rate to a flux. For this purpose, we measured the power-law index in the preceding and following X-ray observation ($\Gamma = 0.06 \pm 0.15$ and $\Gamma = 0.19 \pm 0.15$, respectively). We then selected the most extreme values within their $1 - \sigma$ error ranges and used WEBPIMMS to convert the count rate to a minimum and maximum flux. We select the average of those as the measured flux and refer to the range as the systematic error in Table 2. Finally, we also include the Poisson error on the count rate. Secondly, the ninth radio epoch was surrounded by two *Swift*/XRT observations with approximately the same time difference of ∼1.3 d. Therefore, we fitted both spectra and measured fluxes for both observations. We measure consistent fluxes in these two observations; in the remainder of this work, we adopt the value of the X-ray observation

taken after the radio epoch (ObsID 0001097024, ignoring ObsID 0001097023).

3.4 Short time-scale variability

Given the flaring behaviour of Sw J1858 in both X-ray and optical bands, we set out to investigate whether similar extreme variability is present at radio frequencies. Therefore, we imaged the radio counterpart at both observing frequencies on a 5/3 min (ATCA/VLA) time-scale. Time resolving at this time-scale allowed us to study quick changes in both flux and spectral index, without the increased uncertainties masking any variability. In Figs 3, 4, and 5, we show the resulting light curves for each epoch. We then calculated the spectral index α in each time bin, shown in Figs 3, 4, and 5 as well. The
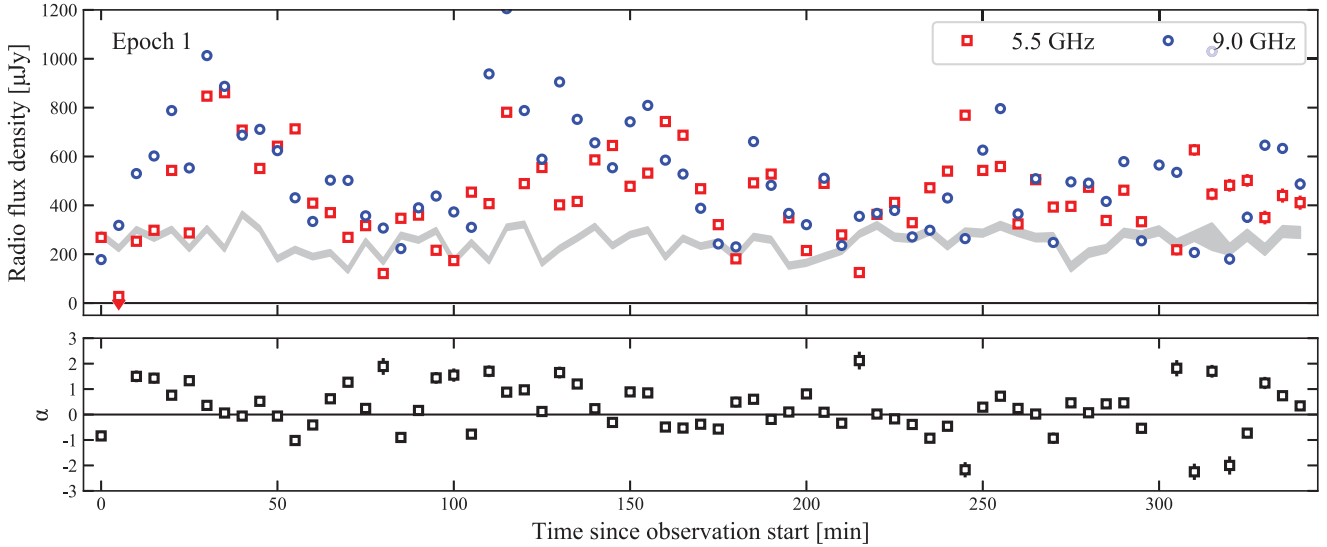
Figure 3. Light curves of the 5.5 (red squares) and 9.0 (blue circles) GHz flux density and the radio spectral index α at a 5-min resolution, for the ATCA observation (epoch 1). The grey band shows the 9-GHz light curve of the nearby flat-spectrum background source.

VLA light curves also show, in grey, the 1σ bands of the flux density of the nearby background source. These bands show to what extend the image-plane analysis is affected by atmospheric or instrumental effects and vary typically on or slightly above the level of the target flux densities' uncertainties.

The ATCA light curve in Fig. 3 shows a highly variable target at both observing frequencies during the ~6 h observing time. At the start of the observation, a flare is observed, rising and decaying on a time-scale of tens of minutes. During the rise and decay of this flare, the spectral index gradually decays from inverted ($\alpha > 1$) to flat ($\alpha \approx 0$). The flux densities across the observation span a dynamical range of more than four, varying between less than 200 µJy to more than 800 µJy on time-scale of tens of minutes. We stress that we are plotting the statistical error on the flux density only, as determined from the uv-plane fit to the point source, which is of the same order as the image-plane RMS in the averaged observation (i.e. 15 µJy). Therefore, the uncertainties are often smaller than the markers. We also show the light curve of the background source, which gives an indication of the systematic uncertainties on the flux density measurements (assuming it is intrinsically constant).

Turning to the VLA light curves in Fig. 4, we observe significant intrinsic variability compared to the background source at either one or both radio frequencies in most epochs. For instance, epoch 4 shows a sequence of decay, rise, and decay within the single 40-min observation. Alternatively, we observe a clear radio flare in epoch 5, rising from ~200 to ~600 µJy in less than 15 min, than decaying over approximately 20 min. Epoch 8 shows a strong decay at 7.5 GHz, from ~350 µJy down to ~50 µJy in less than 30 min. The variability in the other epochs appears more erratic, of a seemingly stochastic nature. We do not observe any strong flares on the time-scale of ~3 min, i.e. in a single time bin. Due to the image-plane approach for these VLA observations, the uncertainties on the individual measurements are significantly larger than for the ATCA epoch.

With its long total observing time, the final VLA observation (epoch 10; Fig. 5) offers a complementary view to epochs 2 to 9: during this observation, the source was not significantly detected in every 3-min time bin. Particularly around the start of the observation, Sw J1858 hovered around flux densities three times the typical short

time-scale RMS sensitivity. Therefore, we only calculate the spectral index in time bins where the source is significantly detected at both 4.5 and 7.5 GHz. During the second half of the observation, Sw J1858 reaches a steady level above the detection threshold, with a relatively flat spectral index. At that point, it does however not appear significantly more variable than the background source. These results show that the behaviour of Sw J1858 in the 40 min observations during epochs 2–9 is not necessarily stationary and can change quite rapidly.

To assess the level and significance of the radio variability, we calculated the fractional variability F_{var} of the light curves of Sw J1858 at both frequencies, and of the background source, following the description in Vaughan et al. (2003). The fractional variability of a light curve $x(t)$ is defined as $F_{var} = \sqrt{(S^2 - \overline{\sigma_{err}^2})/\overline{x}^2}$, where S^2 is the light-curve variance and $\overline{\sigma_{err}^2}$ is the mean square error on the count rate. The calculated values of F_{var} are listed in Table 3. For all epochs but 1, 8, and 10, we observe stronger variability at the lower frequency. In most VLA epochs, the observed fractional variability also exceeds that of the background source, indicating that Sw J1858 was intrinsically variable. In epoch 3 and 5–8, this is the case at both frequencies, while for epochs 4, 9, and 10, only at a single frequency F_{var} significantly exceeds the background source. Only in epoch 2, Sw J1858 and the background source show consistent levels of variability. Note that for epoch 9, F_{var} could not be calculated at 7.5 GHz as the observed variations in flux density where smaller than the average error on the data ($S^2 < \overline{\sigma_{err}^2}$ in the notation of Vaughan et al. 2003). Finally, the much lower uncertainties on the F_{var} measurements for epoch 1 are caused by using only the statistical uncertainty on the uv-plane fit.

In Figs 3, 4, and 5, we also show the radio spectral index as a function of time. We do not observe any optically thin, i.e. $\alpha \approx -0.7$, radio flares, that are associated with the launch of individual ejecta. For instance, in the flare observed at the start of epoch 1, the spectrum is flat to inverted, while during the flare observed in epoch 5, the spectrum is tightly constrained to be flat. With the exception of the decreasing spectral index during the flare in epoch 1, we generally observe little structured evolution in the spectral shape as a function of time, as might for instance result from lags between
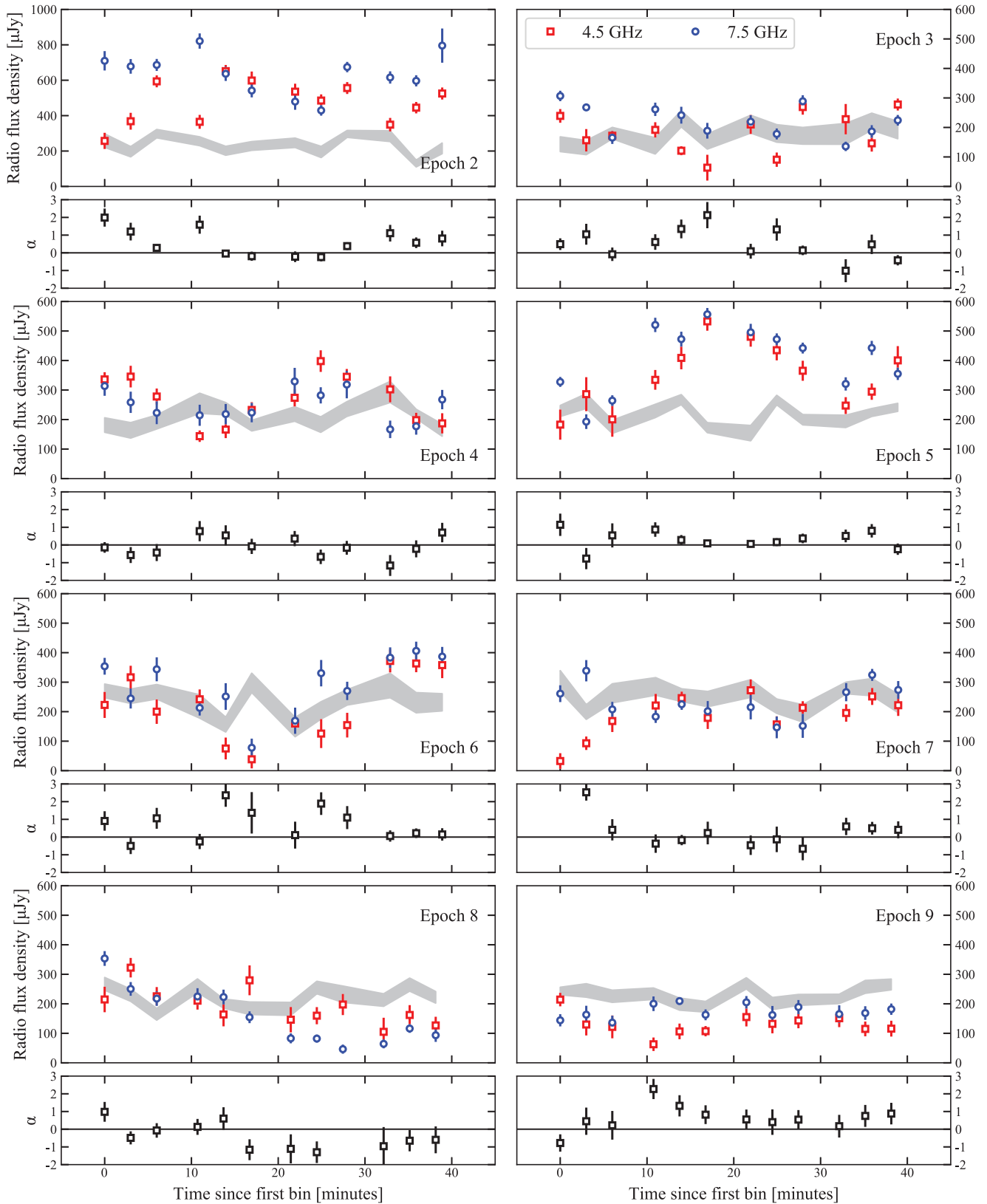
Figure 4. Light curves of the 4.5 (red squares) and 7.5 (blue circles) GHz flux density and the radio spectral index α at a 3-min time resolution, for the first eight VLA observations (epoch 2 – 9). Note the different vertical range in the upper left-hand panel. The spectral index panels correspond to the epoch shown above it. The grey bands show the 1σ band for the background source visible in Fig. 1.
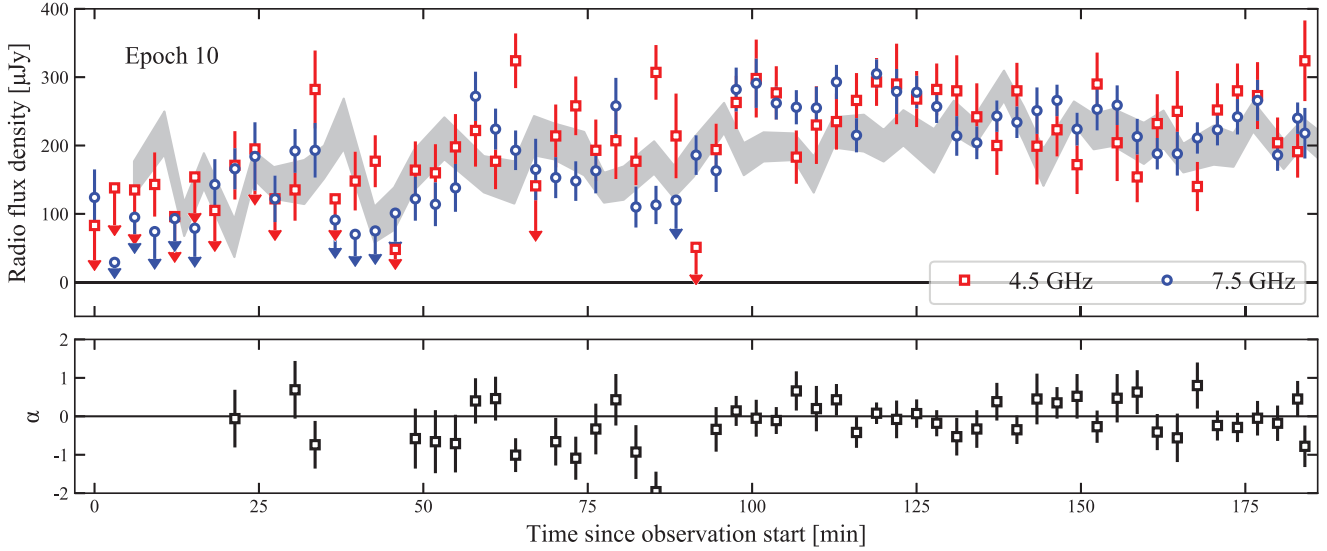
Figure 5. Same as Fig. 4, for epoch 10. Note the difference in observation length with respect to the other VLA epochs. At the start of the observation, the source is not significantly detected in every 3-min time bin; therefore, we only calculate the spectral index α for time bins where the source is detected at both 4.5 and 7.5 GHz.

Table 3. Summary of variability within the X-ray and VLA radio observations. We list the average, minimum, and maximum value of the inferred 6 GHz flux density per epoch, taking both variations in low band flux density and spectral index into account when calculating these values. As an estimate of the radio variability per epoch, we also show the fractional variability F_{var} at both the low (5.5/4.5 GHz for ATCA/VLA) and high (9.0/7.5 GHz) frequency observing band per epoch, and for the background source ('*background*'). Finally, we show the average, minimum, and maximum *Swift*/XRT count rates in 100 s segments. Note that the XRT observations used for epoch 1, 2, and 3 were taken in WT mode, and for epochs 1 and 2 was only 30 s long.

	Inferred 6 GHz radio flux densities (μJy)			Fractional radio variability			*Swift*/XRT count rates (cts s^{-1})		
Epoch	Average	Minimum	Maximum	low-band	high-band	background	Average	Minimum	Maximum
1	435 ± 16	143 ± 16	874 ± 14	37.8 ± 0.5	44.2 ± 0.3	19.0 ± 0.8	0.26 ± 0.01	–	–
2	557 ± 32	453 ± 46	663 ± 93	23.9 ± 2.5 percent	16.7 ± 2.2 percent	17.7 ± 3.7 percent	0.26 ± 0.01	–	–
3	250 ± 16	117 ± 85	280 ± 35	33.7 ± 5.2 percent	21.8 ± 2.8 percent	9.0 ± 7.2 percent	0.10 ± 0.03	0.024 ± 0.01	0.18 ± 0.05
4	282 ± 15	180 ± 37	329 ± 45	28.3 ± 3.4 percent	16.4 ± 4.8 percent	14.8 ± 4.0 percent	0.07 ± 0.01	$0.013^{+0.019}_{-0.009}$	$0.37^{+0.55}_{-0.27}$
5	365 ± 27	229 ± 61	547 ± 41	29.2 ± 3.6 percent	27.0 ± 1.6 percent	15.3 ± 2.8 percent	0.22 ± 0.01	$0.058^{+0.032}_{-0.024}$	0.68 ± 0.13
6	245 ± 24	57 ± 50	387 ± 44	49.0 ± 5.3 percent	32.5 ± 3.8 percent	15.3 ± 4.4 percent	3.19 ± 0.11	$0.06^{+0.03}_{-0.02}$	13.8 ± 1.3
7	204 ± 21	105 ± 86	291 ± 45	33.7 ± 5.1 percent	22.7 ± 4.2 percent	8.9 ± 4.3 percent	3.19 ± 0.11	$0.06^{+0.03}_{-0.02}$	13.8 ± 1.3
8	185 ± 16	80 ± 44	285 ± 73	25.9 ± 6.4 percent	57.7 ± 3.8 percent	12.4 ± 3.2 percent	0.16 ± 0.02	$0.07^{+0.04}_{-0.03}$	0.51 ± 0.08
9	157 ± 19	121 ± 48	182 ± 47	17.0 ± 8.7 percent	–	8.1 ± 3.0 percent	0.16 ± 0.02	0.03 ± 0.02	0.23 ± 0.05
10	171 ± 11	132 ± 47	300 ± 42	23.1 ± 3.5 percent	32.3 ± 2.3 percent	19.0 ± 2.2 percent	0.28 ± 0.01	0.04 ± 0.02	1.17 ± 0.16

the two observing bands. Similarly, we do not find evidence for a relation between the radio flux and spectral shape. Finally, in several epochs, most notably 2, 7, and 8, we observe strongly inverted radio spectra ($\alpha > 2$), turning more flat as the 4.5 GHz flux rises towards the 7.5 GHz flux.

We search for a time delay between the 4.5 and 7.5 GHz light curves using the method described in Section 3.4 of Buisson et al. (2017). To remove the long-term delay during the outburst, we subtracted the mean flux per observation and frequency band. The measured time lag between the full campaign VLA light curves is $\tau = -110 \pm 360$ s, where we quote the 1-sigma uncertainty and positive values imply that the 7.5 GHz band lags behind the 4.5 GHz band. Hence, the observations are consistent with no time lag between the two frequencies.

Finally, since strong variability is also observed in X-rays, we investigated whether the levels of X-ray and radio variability in Sw J1858 could be linked. For this purpose, we extracted 100 s time resolution 0.5–10 keV light curves of all *Swift* observations listed in Table 1, except for the 30 s observation 00010955003 – which means that we do not include epoch 1 and 2 in this comparison. We then

calculated the fractional X-ray variability, which we compared with the radio variability in Fig. 6. From this comparison we can see that no clear relation exists between the fractional variability in X-ray and at either radio observing frequency. We do note that the X-ray and radio observations were not performed simultaneously but merely as close as available, and the final observation (epoch 10) shows that the radio variability can even change within two consecutive segments of 40 min.

3.5 The X-ray – radio luminosity plane

Finally, we turn to the X-ray – radio luminosity plane of hard-state X-ray binaries. While Sw J1858 did not reside in a classical hard state, this figure can offer a comparison with jets from other X-ray binaries, especially in terms of radio luminosity. As these radio luminosities are plotted at 6 GHz in our comparison sample, we calculated 6-GHz flux densities using the 4.5 GHz flux density and the spectral index for the VLA observations. We propagated the errors on both and list the resulting luminosities in Table 3. In Fig. 7, we show the resulting X-ray – radio luminosity plane, showing Sw J1858
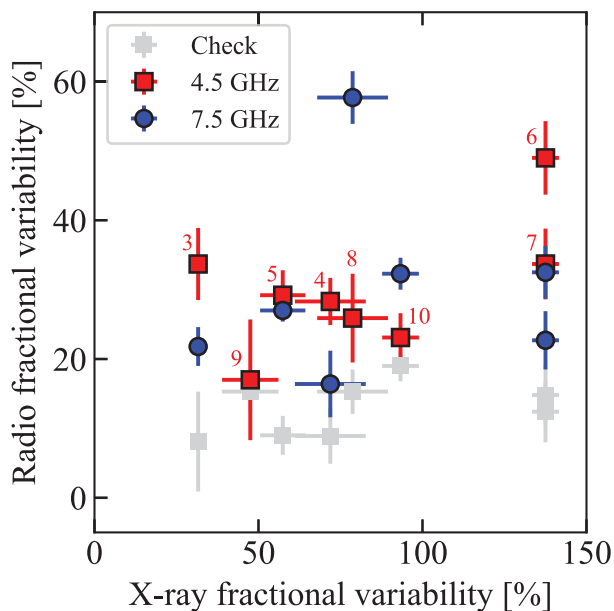
Figure 6. A comparison of the fractional variability in radio and X-ray at a 3-min and 100 s time resolution, respectively. The red numbers correspond to the epoch number. The grey points indicate the background source, showing the typical level of variability that is not intrinsic to Sw J1858. Note that we plot these grey points as a function of X-ray fractional variability of Sw J1858, as no X-ray observations of the background source were taken.

alongside the sample collected in Gallo et al. (2018).[4] The assumed distance of 15 kpc (Buisson et al. 2020b) might be overestimated due to the effects of obscuration by local material, which would move Sw J1858 slightly in the bottom left-hand direction.

Compared to other neutron star systems, Sw J1858 is radio brighter: it overlaps more with the black hole sample, that is systematically radio brighter than the neutron star sample at a given X-ray luminosity (Migliari & Fender 2006; Gallo et al. 2018). However, this might be an effect of strong local absorption in the system: as we will discuss in Sections 4.1 and 4.4, such absorption can be invoked to explain the strong optical and X-ray flaring. In the X-ray – radio luminosity plane, intrinsic absorption moves the source to lower X-ray luminosities, making it appear more radio bright compared to other sources at those luminosities. Hints for this effect might be visible in the two X-ray brightest points, which show a similar radio luminosity as the X-ray fainter observations and are therefore more consistent with other neutron star observations. Alternatively, radio luminosity differences between sources might arise from distinct boosting factors of jets viewed at different inclinations (Motta, Casella & Fender 2018). However, the two X-ray brightest points argue against such a scenario in Sw J1858, as these two radio observations are not significantly radiobrighter than the neutron star sample.

From the figure, no clear correlation between the X-ray and radio luminosity can be distinguished: the radio luminosities remain similar despite a jump in *observed* X-ray luminosity by a factor ~10 in epochs 7 and 8. However, several effects could mask an X-ray – radio coupling, if it were present. First, if local absorption not only reduces the X-ray luminosity but also changes between epochs, the shape of any correlation between X-ray and radio will

[4]The comparison sample from Gallo et al. (2018) can also be found on https://jakobvdeijnden.wordpress.com/radioxray/

also be altered. Secondly, the X-ray and radio observations were not taken simultaneously. Given the strong variability observed *between Swift* observations, the source likely changed in X-ray luminosity significantly during the time separating the VLA and *Swift* observations. Finally, both the X-rays and radio show significant variability *during* the observations, which is not reflected by plotting only the average X-ray and radio luminosities.

To quantify the range in radio luminosity spanned by each epoch, we calculated the inferred 6 GHz flux density in every 3-min time bin, and selected the minimum and maximum value. In X-rays, where we could not obtain sufficient spectral information on short time-scales, we consider count rates[5]: for each epoch, we selected the average count rate, and the minimum and maximum count rates on a time scale of 100 s. We then estimated the range in X-ray luminosity by multiplying the average luminosity by the ratios of minimum versus average and maximum versus average count rates. Finally, we plotted the results of this exercise in Fig. 8. Here, the error bars reflect the range in X-ray and radio luminosity spanned during the epoch. Taking this range into account, the epochs now overlap in both X-ray and radio luminosity, showing that the variability washes out any correlations or coupling that might be observed in strictly simultaneous observations.

Finally, we stress that the high radio to X-ray luminosity ratio and lack of observed luminosity coupling discussed above, stand out mostly in comparison to hard state X-ray binaries. The radio jet of Sw J1858 appears to be of the compact type, determined from its inverted ($\alpha > 0$) observation-averaged spectral index, as seen in the other hard state sources as well. However, from an X-ray point of view, Sw J1858 did not reside in a classical hard state. Therefore, in addition to the effects of variability and obscuration discussed above, the difference in X-ray state also likely contributes to the deviant behaviour of Sw J1858. We discuss this in more detail in Section 4.4.

4 DISCUSSION

4.1 X-ray spectral modelling

To determine the *observed* X-ray flux around the time of the radio observations, we fitted the closest *Swift*/XRT spectrum in time with a phenomenological power law model. For several reasons, this model does not provide a full physical description of the X-ray spectrum; first, we fix the interstellar hydrogen column density to zero, as the fitted value of the absorption pegged at this lower limit. Secondly, the source is highly variable in X-rays, with strong spectral changes during flares (Hare et al. 2020). Finally, as noted first by Reynolds et al. (2018), the spectral shape signals significant local absorption with a more complicated underlying spectral shape, similar to V404 Cyg (Motta et al. 2017) and V4641 Sgr (Maitra & Bailyn 2006; Morningstar et al. 2014).

One of the *Swift*/XRT observations fitted in this work (ObsID 10955004; epoch 3) was analysed by Reynolds et al. (2018) with a more complicated partial covering model: PHABS ∗ (BAPEC + PCFABS∗PO). They measure a 0.5–10 keV flux, corrected for ISM absorption but *not* local absorption by the partial covering, consistent with the power-law estimate. The intrinsic power-law flux, corrected for partial covering, is however a factor ~4 higher. To extend this

[5]In other words, we effectively assume a constant spectral shape during each *Swift* observation, independent of flux or flaring. We note that this is an oversimplification, as the spectral shape could change during flares.
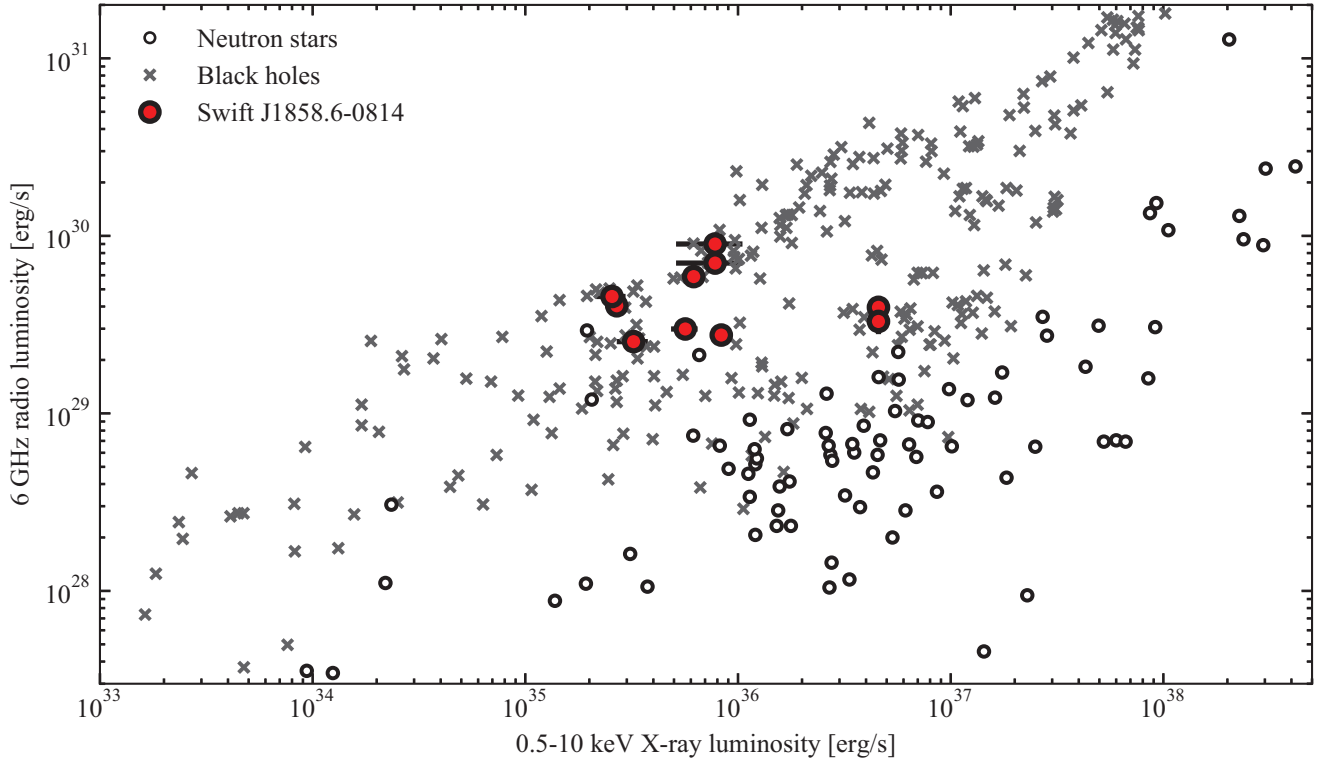
Figure 7. The X-ray – radio luminosity plane for black hole and neutron star X-ray binaries. The grey crosses show black hole (candidates), while the circles show different classes of accreting neutron stars. We show the average 0.5–10 keV X-ray and inferred 6-GHz radio luminosities of Sw J1858 for a 15 kpc distance. The two brightest radio points are epochs 1 and 2, which share the same X-ray observation. Note that the errors do not reflect the variability within observations, nor account for the non-simultaneity of the X-ray and radio observations and the variability between *Swift* observations (Section 3.5). The comparison sample was taken from Gallo, Degenaar & van den Eijnden (2018).
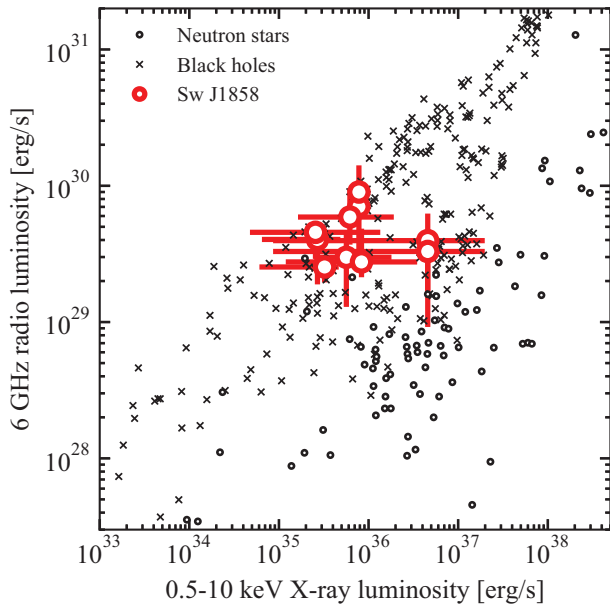

Figure 8. The X-ray – radio luminosity plane with Sw J1858 shown in red circles. Here, the error bars reflect the variability range in X-ray count rate (on 100 s time-scales) and radio flux density (on 3 min time-scales) during each observation.

comparison between the two models, we also fitted the brightest (both in flux and total counts) *Swift*/XRT epochs (ObsId 10955008) with the partial covering model. Again, we find consistent values for the locally absorbed flux (i.e. only ISM corrected), while the intrinsic power-law flux is a factor ∼2.3 higher (i.e. after correcting for local absorption) in the 0.5–10 keV range.

The low flux of Sw J1858 prevents us from a systematic analysis of all *Swift*/XRT spectra with the more complicated intrinsic absorption model of Reynolds et al. (2018) – when trying such an analysis, we find poorly constrained and highly degenerate spectral parameters. However, the above considerations show that using a non-physical power-law model results in similar measurements of the *observed* fluxes. Similarly, we find that local absorption only alters the measured flux by a factor of roughly 2–4, which is within the systematic uncertainty introduced by the X-ray flaring (see e.g. Fig. 8). We will discuss the effects of local absorption in more detail in Section 4.4.

4.2 The origin of radio variability of Sw J1858

In this section, we will discuss what might cause the observed radio variability in Sw J1858. First, could it be caused by changes in the geometry of the jet, such as precession, leading to a variable jet boosting factor? Jet precession has been directly observed (Coriat et al. 2019; Miller-Jones et al. 2019) or inferred (e.g. Gallo et al. 2014) in several LMXBs, and has been proposed as the mechanism behind quasi-periodic oscillations in X-rays at (sub-)second time-scales (Stella & Vietri 1998; Ingram, Done & Fragile 2009; Ingram et al. 2016). However, we do not find any evidence for precession

in our observations: most of the radio variability appears to be stochastic, and the exceptions, such as the radio flare in epoch 5, do not show (quasi)-periodic variations. Therefore, we rule out such a scenario.

Secondly, we can consider whether radio intensity scintillation caused by scattering in the interstellar medium might contribute to the observed variations in Sw J1858. Following Pandey et al. (2006), we use the online NE2001 tool[6] by Cordes & Lazio (2001) to calculate the scintillation characteristics in the direction of Sw J1858, for several distances. For all observing frequencies, the predicted time-scales for amplitude variations due to scintillation are shorter than our time resolution. The affected angular size scales are of the order of 50–100 µas. At 15 kpc, this size translates to a scale of $5–10 \times 10^7$ gravitational radii for a $1.4 \, M_\odot$ neutron star. It is (particularly for neutron star X-ray binaries) poorly known from what physical distances from the accretor the cm-wavelength radio emission originates. For black holes, the recent correlated X-ray and radio timing study of Cyg X-1 suggests similar or larger scales than those affected by scintillation (Tetarenko et al. 2019a). However, due to the mismatch in time-scales, we consider it unlikely that scintillation contributes significantly to the observed variability.

Thirdly, the radio variability does not appear to be caused by the launch of discrete ejecta. The launch of such ejecta has been associated with strong radio variability as observed in both V404 Cyg (Tetarenko et al. 2017) and V4641 Sgr (Rupen et al. 2003a, 2004a; Rupen, Mioduszewski & Dhawan 2003b, 2004b) during states of extreme X-ray flaring, similar to that seen in Sw J1858. In Sw J1858, we do not observe the steady, optically thin spectra associated with a bright (or decaying) radio flare that are expected in this scenario; indeed, during the flares observed in epochs 1 and 5, the radio spectrum is flat or inverted during the peak. Also, we do not see a smoothing of the variability towards lower frequencies, as observed in this scenario (e.g. Tetarenko et al. 2017). Similarly, we find no evidence that the radio variability is directly related to the contemporaneous level of X-ray flaring. While the radio and X-ray observations are not strictly simultaneous, we do not find a relation between the fractional variability in X-rays and radio. This direct relation between the X-ray and radio flaring was neither observed in V404 Cyg (Tetarenko et al. 2017). This is consistent with a scenario where the X-ray flaring is caused by strong obscuration of the inner accretion flow combined with a high mass accretion rate (See Section 4.4), as the obscuration would not affect the jet.

Alternatively, the radio variability might be caused by intrinsic variability in the accretion flow and mass accretion rate propagating into the jet (e.g. Malzac 2014). This scenario can explain why the radio spectrum remains, on average, inverted over time, as the compact jet does not change its global morphology. We observe that the variability is stronger, in most observations, at the lower observing frequency. This difference in variability could arise if the fluctuations are smeared out to longer time-scales further down the jet, at lower emission frequencies, therefore better matching the 3 to 5 min time-scales probed by our analysis. Using simultaneous X-ray and radio observations, Tetarenko et al. (2019a) showed that a similar scenario is at play in Cyg X-1. However, without simultaneous X-ray coverage of, for instance, the flare in epoch 5, it is challenging to directly show how the intrinsic variability propagates from the accretion flow to the jet.

The variability in the accretion flow could arise from, for instance, the mass accretion rate fluctuations in the disc that are typically used

to explain rapid broad-band X-ray variability (Ingram & Done 2011; Rapisarda et al. 2016). Alternatively, disc tearing due to Lense–Thirring precession, caused by a misalignment between the accretor and disc spin axis, was proposed by Nixon & King (2012) and Nixon et al. (2012) to cause variations in the accretion rate. To test whether the latter scenario could contribute, we can estimate the minimum required spin misalignment for Sw J1858. Neutron stars in LMXBs have typical dimensionless spin parameters a between ∼0.05 and 0.25, for a range of equations of state (Haensel et al. 2009; Lo & Lin 2011). We assume a standard viscous disc with $\alpha = 0.1$ and a moderately vertically extended flow ($H/R \approx 0.1$), valid if the Sw J1858 is intrinsically accreting at higher rates than observed (see Section 4.4). Then, from equation (9) in Nixon et al. (2012), we find that the spins must be misaligned by at least 8.6° (1.7°) for $a = 0.25$ ($a = 0.05$). If we add a second requirement, namely that the disc must tear at a radius larger than the neutron star radius (assumed to be 10 km), we find that the misalignment angle must be >14° for $a = 0.25$, and even larger for smaller spins. The detection of Type-I bursts in Sw J1858 suggest a relatively weak magnetic field; therefore, such a spin misalignment should have persisted while the magnetic field decayed, in order for this scenario to be feasible.

4.3 Sw J1858 in the L_X–L_R diagram: the effects of variability

Here, we briefly turn to the behaviour of Sw J1858 in the X-ray – radio luminosity plane and the effects of X-ray and radio variability. We first re-emphasize that Sw J1858 was not observed in the canonical hard X-ray state, where the other sources in the L_X–L_R diagram reside. Therefore, it is not surprising that we do not observe a clear coupling between the X-ray and radio luminosity: such a coupling is also not observed during flaring states of the black holes V404 Cyg (Tetarenko et al. 2017, 2019b) or GRS 1915+105 (Pooley & Fender 1997). Similarly, one cannot easily state whether Sw J1858 is underluminous compared to the sample, even if it intrinsically accretes at higher rates (see Section 4.4).

Recently, Plotkin et al. (2019) analysed all quiescent observations of V404 Cyg, focusing on the variability properties in the radio and X-ray band. They showed that, while the source shows a correlation between its X-ray and radio luminosity during the non-flaring states, this correlation disappears when accounting for intra-observational variability and non-simultaneity between X-ray and radio observations. We similarly find that, when plotting the full range in X-ray and radio luminosities reached in an observation, different epochs overlap in the L_X–L_R diagram. So while we do not observe an X-ray – radio coupling during the time-averaged observations, any such coupling detected would not have been reliable given the level of observed variability.

4.4 A radio comparison between Sw J1858 and Eddington-limited LMXBs

In the black hole LMXBs V404 Cyg and V4641 Sgr, the observed strong optical and X-ray flaring can be explained by an extreme, ∼Eddington mass accretion rate, combined with a high inclination (e.g. Wijnands & van der Klis 2000; Muñoz-Darias et al. 2016; Motta et al. 2017; Sánchez-Fernández et al. 2017). Due to the high mass accretion rate, the inner accretion flow puffs up into a vertically extended flow, launching a highly ionized and clumpy outflow. As a result, the inner accretion flow is typically blocked from view, reducing the observed X-ray flux greatly, with brief intervals providing an unobscured view causing the large flares. As similarly strong flaring is observed in the X-ray and optical bands in the

neutron star Sw J1858 (Baglio et al. 2018; Ludlam et al. 2018; Paice et al. 2018; Rajwade et al. 2018, 2019; Vasilopoulos et al. 2018; Hare et al. 2019; Hare et al. 2020), a similar scenario might be at play in the accretion flow there (although see Hare et al. 2020, for a recent discussion on possible differences between the X-ray behaviour of V404 Cyg, V4641 Sgr, and Sw J1858). Do the radio (variability) properties of Sw J1858 fit with such high-inclination, highly obscured, Eddington-limited accretion?

The recent report by Buisson et al. (2020b) of the detection of Type-I bursts in Sw J1858 shows the presence of a neutron star primary. Therefore, here, we first consider whether Eddington-limited accretion in such a neutron star LMXB might explain the observed radio behaviour in Sw J1858. The neutron star LMXBs with the highest mass accretion rates are the Z-sources, which are thought to accrete near or at the Eddington luminosity, tracing out Z-shaped tracks in their X-ray colour–colour diagrams (Hasinger & van der Klis 1989; Homan et al. 2010). Z-sources can show strong changes in radio brightness, related to the branch they are positioned on in their colour–colour diagram track; they are radio brighter and more variable in the Horizontal Branch than in the Flaring and Normal Branches (Penninx et al. 1988; Hjellming et al. 1990a,b; Spencer et al. 2013; Motta & Fender 2019). Time-resolved radio studies of the different branches in Sco X-1 by Hjellming et al. (1990b) and Cyg X-2 by Hjellming et al. (1990a) show that these sources have similar levels of radio variability and luminosity to Sw J1858 during their radio-faint Flaring and lower Normal Branches. However, in the X-ray – radio luminosity plane, these sources are located to the right of Sw J1858, around the neutron star Eddington limit of $2 \times 10^{38} \, \mathrm{erg \, s^{-1}}$. For Sw J1858 to be similar to these sources, it would therefore have to be viewed a high inclination, reducing its observed X-ray flux and masking the Z-source variability properties through obscuration. However, a clear radio difference between Sw J1858 and the Z-sources is the radio spectral index: contrary to Sw J1858, Z-sources typically show steep spectra and are indeed associated with the launch of (resolved) discrete ejecta (Motta & Fender 2019). Also, in this scenario, Sw J1858 should not have resided in the much more radio bright Horizontal Branch during any of the observations, which is unlikely given the time-scales and commonness of transitions between the branches (Homan et al. 2010).

We can alternatively make the comparison with the black hole V404 Cyg, which was extensively monitored in the X-ray and radio bands during its 2015 outburst. At the peak of its Eddington-limited outburst, it showed a strongly flaring X-ray state (Motta et al. 2017; Sánchez-Fernández et al. 2017) in which the observed radio variability – flaring up to flux densities of 1 Jy – is associated with the launch of discrete ejecta (Tetarenko et al. 2017). As it decayed towards quiescence, V404 Cyg transitioned into a more calm state where a compact, but still variable (albeit at a lower level) radio jet starts to dominate the radio emission at the level of several mJy (Tetarenko et al. 2019b). In addition, in the first several days of the outburst, before the peak, the X-ray band already showed flaring while AMI-LA radio monitoring reveals a relative faint and variable radio source at tens to hundreds of mJy (Muñoz-Darias et al. 2016).

While the peak of the V404 Cyg outburst might resemble the X-ray behaviour of Sw J1858 most closely, the radio properties of both sources do not match in this state: Sw J1858 does not show evidence for optically thin, discrete ejecta, and is significantly underluminous compared to V404 Cyg in this state. In terms of levels of radio variability, radio spectral index, and radio luminosity, Sw J1858 is in fact more similar to the behaviour of V404 Cyg during the decay of its 2015 outburst: a large distance of 15 kpc to Sw J1858 can account for

the difference in radio flux density, and both sources show an inverted spectrum. In addition, Tetarenko et al. (2019b) suggest that the radio variability observed in this state have propagated down the jet from the accretion flow, as we suggest for Sw J1858. However, during this state, the X-ray behaviour does not match: at that point, the X-ray flaring had halted in V404 Cyg. That leaves the very start of the outburst. Again, for the Type-I burst distance to Sw J1858 of 15 kpc, the radio luminosities are similar, while V404 Cyg already showed X-ray flaring at this point (Muñoz-Darias et al. 2016). Comparing the radio variability properties is however difficult, as the detailed variability studies by Tetarenko et al. (2017, 2019b) of V404 Cyg do not include the AMI-LA observations from this part of the outburst. Also, a clear difference in this scenario is the duration: this short lived state in the 2015 outburst of V404 Cyg was followed by the radio-flaring outburst peak only days later, while in Sw J1858, the same behaviour has persisted for months (see Fig. 2).

5 CONCLUSIONS

In this paper, we have reported radio monitoring of the new transient neutron star X-ray binary Sw J1858. While the source does not show a canonical hard state, we detect a compact jet in every observation. Time-resolving the observations, we find that the jet emission is highly variable in most observations. Finally, we do not observe a clear correlation between the radio and X-ray luminosity of Sw J1858, as also seen in other LMXBs showing similar flaring X-ray states. We find that the radio variability is most likely associated with a compact jet responding to variations in the accretion flow propagating down the jet. Precession, scintillation, and the launch of discrete ejecta can be ruled out as possible explanations. Finally, we discuss how the radio properties of Sw J1858 compare to other LMXBs showing similar X-ray flaring behaviour, finding that none of these previously observed sources provides a perfect match. Therefore, while several of the radio properties of Sw J1858 are similar to either Z-sources, V404 Cyg or V4641 Sgr, it also shows as-of-yet unseen behaviour.

[7] http://www.astropy.org

Telescope, which is funded by the Commonwealth of Australia for operation as a National Facility managed by CSIRO. The National Radio Astronomy Observatory is a facility of the National Science Foundation operated under cooperative agreement by Associated Universities, Inc.

The data underlying this article are available in Zenodo, at https://dx.doi.org/10.5281/zenodo.3878127.

REFERENCES

Allen J. L., Schulz N. S., Homan J., Neilsen J., Nowak M. A., Chakrabarty D., 2018, ApJ, 861, 26

Astropy Collaboration, 2013, A&A, 558, A33

Baglio M. C., Russell D. M., Pirbhoy S., Bahramian A., Heinke C. O., Roche P., Lewis F., 2018, Astron. Telegram, 12180, 1

Blandford R. D., Königl A., 1979, ApJ, 232, 34

Bozzo E., Ferrigno C., Savchenko V., Ducci L., Kuulkers E., 2018, Astron. Telegram, 12167, 1

Bright J., Fender R., Motta S., Rhodes L., Titterington D., Perrott Y., 2018, Astron. Telegram, 12184, 1

Buisson D. J. K., Lohfink A. M., Alston W. N., Fabian A. C., 2017, MNRAS, 464, 3194

Buisson D. J. K., Altamirano D., Remillard R., Arzoumanian Z., Gendreau K., Gandhi P., Vincentelli F., 2020a, Astron. Telegram, 13536, 1

Buisson D. J. K. et al., 2020b, Astron. Telegram, 13563, 1

Cash W., 1979, ApJ, 228, 939

Charles P., Matthews J. H., Buckley D. A. H., Gandhi P., Kotze E., Paice J., 2019, MNRAS, 489, L47

Corbel S., Fender R. P., Tzioumis A. K., Nowak M., McIntyre V., Durouchoux P., Sood R., 2000, A&A, 359, 251

Corbel S., Fender R. P., Tomsick J. A., Tzioumis A. K., Tingay S., 2004, ApJ, 617, 1272

Cordes J. M., Lazio T. J. W., 2001, ApJ, 549, 997

Coriat M., Fender R. P., Tasse C., Smirnov O., Tzioumis A. K., Broderick J. W., 2019, MNRAS, 484, 1672

Corral-Santana J. M., Casares J., Muñoz-Darias T., Bauer F. E., Martínez-Pais I. G., Russell D. M., 2016, A&A, 587, A61

Dhawan V., Mirabel I. F., Rodríguez L. F., 2000, ApJ, 543, 373

Díaz Trigo M. et al., 2018, A&A, 616, A23

Done C., Gierlinski M., Kubota A., 2007, A&AR, 15, 1

Evans P. A., et al., 2007, A&A, 469, 379

Evans P. A. et al., 2009, MNRAS, 397, 1177

Fender R. P., Belloni T. M., Gallo E., 2004, MNRAS, 355, 1105

Fender R. P., Homan J., Belloni T. M., 2009, MNRAS, 396, 1370

Fomalont E. B., Geldzahler B. J., Bradshaw C. F., 2001a, ApJ, 553, L27

Fomalont E. B., Geldzahler B. J., Bradshaw C. F., 2001b, ApJ, 558, 283

Gallo E. et al., 2014, MNRAS, 445, 290

Gallo E., Degenaar N., van den Eijnden J., 2018, MNRAS, 478, L132

Galloway D. K., Keek L., 2017, preprint (arXiv:1712.06227)

Gehrels N. et al., 2004, ApJ, 611, 1005 (Swift)

Gusinskaia N. V. et al., 2017, MNRAS, 470, 1871

Haensel P., Zdunik J. L., Bejger M., Lattimer J. M., 2009, A&A, 502, 605

Hare J., Gandhi P., Paice J. A., Tomsick J., 2019, Astron. Telegram, 12512, 1

Hare J. et al., 2020, ApJ, 890, 57

Hasinger G., van der Klis M., 1989, A&A, 225, 79

Higginbottom N., Proga D., Knigge C., Long K. S., 2017, ApJ, 836, 42

Hjellming R. M., Han X. H., Cordova F. A., Hasinger G., 1990a, A&A, 235, 147

Hjellming R. M. et al., 1990b, ApJ, 365, 681

Homan J. et al., 2010, ApJ, 719, 201

Homan J., Neilsen J., Allen J. L., Chakrabarty D., Fender R., Fridriksson J. K., Remillard R. A., Schulz N., 2016, ApJ, 830, L5

Ingram A., Done C., 2011, MNRAS, 415, 2323

Ingram A., Done C., Fragile P. C., 2009, MNRAS, 397, L101

Ingram A., van der Klis M., Middleton M., Done C., Altamirano D., Heil L., Uttley P., Axelsson M., 2016, MNRAS, 461, 1967

Jiménez-Ibarra F., Muñoz-Darias T., Casares J., Armas Padilla M., Corral-Santana J. M., 2019, MNRAS, 489, 3420

Kalemci E., Tomsick J., Buxton M., Rothschild R., Pottschmidt K., Corbel S., Brocksopp C., Kaaret P., 2005, ApJ, 622, 508

Kennea J. A., Krimm H. A., 2018, Astron. Telegram, 12160, 1

Krimm H. A. et al., 2018, Astron. Telegram, 12151, 1

Lewin W., van Paradijs J., Taam R., 1995, in Lewin W. H.G ., van Paradijs J., van den Heuvel E. P. J., eds, X-Ray Binaries. Cambridge Univ. Press, Cambridge, p. 175

Lo K. W., Lin L. M., 2011, ApJ, 728, 12

Ludlam R. M. et al., 2018, Astron. Telegram, 12158, 1

Ludlam R. M. et al., 2019, ApJ, 873, 99

Maitra D., Bailyn C. D., 2006, ApJ, 637, 992

Malzac J., 2014, MNRAS, 443, 299

Martí-Vidal I., Vlemmings W. H. T., Muller S., Casey S., 2014, A&A, 563, A136

McMullin J. P., Waters B., Schiebel D., Young W., Golap K., 2007, in Shaw R. A., Hill F., Bell D. J., eds, ASP Conf. Ser. Vol. 376, CASA Architecture and Applications. Astron. Soc. Pac., San Francisco, p. 127

Migliari S., Fender R., 2006, MNRAS, 366, 79

Miller-Jones J. et al., 2010, ApJ, 716, L109

Miller-Jones J. C. A. et al., 2019, Nature, 569, 374

Morningstar W. R., Miller J. M., Reynolds M. T., Maitra D., 2014, ApJ, 786, L20

Motta S. E., Fender R. P., 2019, MNRAS, 483, 3686

Motta S. E. et al., 2017, MNRAS, 471, 1797

Motta S. E., Casella P., Fender R. P., 2018, MNRAS, 478, 5159

Muñoz-Darias T. et al., 2016, Nature, 534, 75

Muñoz-Darias T., Torres M. A. P., Garcia M. R., 2018, MNRAS, 479, 3987

Muñoz-Darias T. et al., 2019, ApJ, 879, L4

Muñoz-Darias T. et al., 2020, ApJ, 893, L19

Neilsen J., Lee J., 2009, Nature, 458, 481

Nixon C. J., King A. R., 2012, MNRAS, 421, 1201

Nixon C., King A., Price D., Frank J., 2012, ApJ, 757, L24

Paice J. A., Gandhi P., Dhillon V. S., Marsh T. R., Green M., Breedt E., 2018, Astron. Telegram, 12197, 1

Pandey M., Rao A. P., Pooley G. G., Durouchoux P., Manchanda R. K., Ishwara-Chandra C. H., 2006, A&A, 447, 525

Penninx W., Lewin W. H. G., Zijlstra A. A., Mitsuda K., van Paradijs J., 1988, Nature, 336, 146

Plotkin R. M., Miller-Jones J. C. A., Chomiuk L., Strader J., Bruzewski S., Bundas A., Smith K. R., Ruan J. J., 2019, ApJ, 874, 13

Ponti G., Fender R., Begelman M., Dunn R., Neilsen J., Coriat M., 2012, MNRAS, 422, L11

Ponti G., Morris M., Terrier R., Goldwurm A., 2013, in Torres D., Reimer O., eds, Cosmic Rays in Star-Forming Environments. Advances in Solid State Physics. Springer-Verlag, Berlin, Heidelberg, p. 331

Pooley G. G., Fender R. P., 1997, MNRAS, 292, 925

Price-Whelan A. M. et al., 2018, AJ, 156, 123

Rajwade K., Kennedy M., Breton R., Stappers B., Sanpa-arsa S., Irawati P., Dhillon V., Marsh T., 2018, Astron. Telegram, 12186, 1

Rajwade K. M. et al., 2019, Astron. Telegram, 12499, 1

Rapisarda S., Ingram A., Kalamkar M., van der Klis M., 2016, MNRAS, 462, 4078

Reynolds M. T., Miller J. M., Ludlam R. M., Tetarenko B. E., 2018, Astron. Telegram, 12220, 1

Rodriguez J. et al., 2015, A&A, 581, L9

Rupen M. P., Dhawan V., Mioduszewski A. J., 2003a, Astron.Telegram, 175, 1

Rupen M. P., Mioduszewski A. J., Dhawan V., 2003b, Astron. Telegram, 172, 1

Rupen M. P., Dhawan V., Mioduszewski A. J., 2004a, Astron. Telegram, 303, 1

Rupen M. P., Mioduszewski A. J., Dhawan V., 2004b, Astron. Telegram, 296, 1

Russell T. D., Soria R., Miller-Jones J. C. A., Curran P. A., Markoff S., Russell D. M., Sivakoff G. R., 2014, MNRAS, 439, 1390

Sánchez-Fernández C., Kajava J. J. E., Motta S. E., Kuulkers E., 2017, A&A, 602, A40

Spencer R. E., Rushton A. P., Bałucińska-Church M., Paragi Z., Schulz N. S., Wilms J., Pooley G. G., Church M. J., 2013, MNRAS, 435, L48

Stella L., Vietri M., 1998, ApJ, 492, L59

Stirling A. M., Spencer R. E., de la Force C. J., Garrett M. A., Fender R. P., Ogley R. N., 2001, MNRAS, 327, 1273

Strohmayer T., Bildsten L., 2006, in Lewin W., van der Klis M., eds, New Views of Thermonuclear Bursts. Cambridge Univ. Press, Cambridge, UK, p. 113

Tetarenko B. E., Sivakoff G. R., Heinke C. O., Gladstone J. C., 2016, ApJS, 222, 15

Tetarenko A. J. et al., 2017, MNRAS, 469, 3141

Tetarenko A. J., Casella P., Miller-Jones J. C. A., Sivakoff G. R., Tetarenko B. E., Maccarone T. J., Gand hi P., Eikenberry S., 2019a, MNRAS, 484, 2987121

Tetarenko A. J. et al., 2019b, MNRAS, 482, 2950

van den Eijnden J. et al., 2019, MNRAS, 487, 4355

Vasilopoulos G., Bailyn C., Milburn J., 2018, Astron. Telegram, 12164, 1

Vaughan S., Edelson R., Warwick R. S., Uttley P., 2003, MNRAS, 345, 1271

Verner D., Ferland G., Korista K., Yakovlev D., 1996, ApJ, 465, 487

Wijnands R., van der Klis M., 2000, ApJ, 528, L93

Wilms J., Allen A., McCray R., 2000, ApJ, 542, 914

[1] *Anton Pannekoek Institute for Astronomy, University of Amsterdam, Science Park 904, NL-1098 XH Amsterdam, the Netherlands*
[2] *Physics and Astronomy, University of Southampton, Southampton, Hampshire SO17 1BJ, UK*
[3] *Instituto de Astrofísica de Canarias, E-38205 La Laguna, Tenerife, Spain*
[4] *Departamento de Astrofísica, Universidad de La Laguna, E-38206 La Laguna, Tenerife, Spain*
[5] *Department of Physics and Astronomy, Michigan State University, East Lansing, MI 48824, USA*
[6] *International Centre for Radio Astronomy Research, Curtin University, GPO Box U1987, Perth, WA 6845, Australia*
[7] *Facultad de Ciencias Astronómicas y Geofísicas, Universidad Nacional de La Plata, Paseo del Bosque s/n, 1900 La Plata, Argentina*
[8] *Instituto Argentino de Radioastronomía (CCT-La Plata, CONICET; CI-CPBA), C.C. No. 5, 1894 Villa Elisa, Argentina*
[9] *Department of Physics, CCIS 4-183, University of Alberta, Edmonton, AB T6G 2E1, Canada*
[10] *Department of Physics, Box 41051, Science Building, Texas Tech University, Lubbock, TX 79409-1051, USA*
[11] *Department of Physics and Astronomy, Wheaton College, Norton, MA 02766, USA*
[12] *Department of Astronomy and Astrophysics, Atatürk University, Erzurum, Turkey*
[13] *Center for Astro, Particle and Planetary Physics, New York University Abu Dhabi, PO Box 129188 Abu Dhabi, UAE*
[14] *Department of Physics, University of Nevada, Reno, 1664 N. Virginia Street Reno, NV 89557, USA*
[15] *East Asian Observatory, 660 N. A'ohōkū Place, University Park, Hilo, HI 96720, USA*

This paper has been typeset from a TEX/LATEX file prepared by the author.